

Variability analysis of the systematic biases in satellite precipitation estimation related to cloud microphysics and radiative properties

Izabelly C. Costa¹, Christian Kummerow², Luiz. A. T. Machado¹, David Randel², Veljko Petkovic^{2,4} and Sarah Ringerud³

¹ National Institute for Space Research - INPE, Center for Weather Forecast and Climate Studies
- CPTEC, Rodovia Presidente Dutra, km 40.

² Department of Atmospheric Science, Colorado State University, Fort Collins, Colorado

³ Hydrological Sciences Laboratory, NASA Goddard Space Flight Center, Greenbelt, Maryland

⁴ Earth System Science Interdisciplinary Center, College Park, Maryland, United States

* Corresponding author: Tel.: + 55 12 31868602.

E-mail address: izabelly.costa@inpe.br

Abstract

South America extends through a wide range of latitudes, from 12° N to 55° S, and has a varying topography, favoring a diverse meteorological systems and, consequently, a climatic inhomogeneity in the countries. In the area selected for this study, from the Andean mountain range to the Brazilian northeast coast and from 1° N to 9° S, different meteorological systems are encountered. Variations of the macro- and microphysical parameters of clouds becomes important when satellite precipitation is to be estimated or evaluated in an area with such diverse precipitation systems. In this study, one year of Global Precipitation Measurement (GPM) core satellite observations (September 2014 to August 2015), over four diverse regions, is used to assess the consistency in the ice aloft to the surface precipitation relationship. The rain rate and ice water path (IWP) are determined by the GPM combined algorithm, while a GPM radiometer (GMI) is used to provide additional information on potential sources of diagnosed errors. Analyses are carried out to reflect the dependence on changes in region, season, and precipitation type. The results suggest an overestimation of the GPM passive microwave precipitation estimates for low values of IWP and an underestimation for larger values of the atmospheric ice column. The relationship between the surface precipitation rate and IWP is found to be consistent both seasonally and spatially. An assessment of the IWP estimate as a function of the brightness temperature revealed the potential for improving the quality of precipitation estimates using satellite passive microwave observations.

Keywords: Satellite rainfall estimation; passive microwave rainfall estimation; microphysics properties.

1. Introduction

Precipitation regimes vary significantly between the different regions of Brazil due to the country's large territory. The total yearly precipitation ranges from 400 mm in the Northeast to 3500 mm in the North (INMET, 2017). Meteorological systems in different regions also display different characteristics, including large variations in the vertical and horizontal extents as well as in system duration.

A large fraction of the total precipitation in the different regions of Brazil is associated with cold fronts, squall lines in tropical and middle latitudes, mesoscale convective systems (MCS), the Intertropical Convergence Zone (ITCZ), easterly waves, the South Atlantic Convergence Zone (SACZ), upper tropospheric cyclonic vortices (UTCV) and local convection, in addition to the interaction of these systems with the topography. In northeast Brazil (NE), three basic precipitation regimes can be identified, each associated with a different rain production system (Molion and Bernardo, 2002). The precipitation regime in the northern part of the NE, which comprises Ceará and areas from Rio Grande do Norte, Piauí, Maranhão and the west of Paraíba and Pernambuco, is influenced by the ITCZ. In the southern section of the NE, which covers a large area of Bahia and the south of Maranhão and Pauí, the precipitation is driven by the South Atlantic Convergence Zone (SACZ), systems formed ahead of cold fronts, local convection and breezes. Finally, the precipitation in the coastal strip from Rio Grande do Norte to the south of Bahia is dominated by easterly waves and the sea breeze. UTCV systems also influence the precipitation regime in southeast (SE) Brazil. Upper tropospheric winds rotate clockwise in UTCV systems, causing dry air from high tropospheric levels to sink toward surface levels. Therefore, the UTCV acts as a dry air mass for regions near the center of the system. On the other hand, the formation of cumulonimbus and other precipitating clouds occurs near the borders of these systems. During the southern hemisphere winter, UTCV systems can be found in the Atlantic Ocean, further away from the Brazilian NE than in summer, when they suffer a displacement toward the American continent.

The ITCZ influences the precipitation regime over the Amazon region in direct and indirect ways. Its seasonal displacement directly acts on the precipitation in the region: higher rain accumulates in the north of Brazil taking place when the ITCZ is in its furthest southern position, while the period with lower precipitation rates and accumulations is associated with a more

northerly position. Indirectly, the ITCZ influences precipitation in two additional ways: through the formation of convective cell clusters along the ITCZ that move westward and can reach the Amazon basin and through squall lines that form due to the interaction of the trade winds with the sea breeze and can reach far inland, in many cases, the Andes (Reboita et al., 2010). MCSs also contribute to precipitation in the Brazilian northern region (Salio et al., 2007). According to Salio et al. (2007), MCSs in the tropics exhibit differences when compared to those in the subtropical regions in terms of size, diurnal cycle and duration. While in the subtropics, MCSs are modulated by synoptic systems, while tropical MCSs are associated with the surface warming by radiative forcing that, in turn, promotes water vapor flux convergence and convection. MCS in the tropics are typically initiated between 1500 and 2100 GMT, with a maximum intensity between 1800 and 0000 GMT, a life cycle of less than 9 hours in 89% of the cases, and with a maximum extent of up to 150000 km².

During the rainy season, at least 20 to 30% of the rain in this region comes from warm clouds (Tavares, 2012). The cloud condensation nuclei (CCN) concentration in the Amazon region decreases in the rainy season, with quantities similar to those observed over the oceans, approximately 200 cm⁻³ at a water vapor supersaturation of 1% (Roberts et al, 2001). Thus, the scarce CCN grow rapidly within a few clouds and precipitate without developing a cold process, resulting in clouds with a low ice content or associated lightning activity (Williams et al., 2002). These clouds also have little time to develop, reaching maximum cloud heights between 4 and 5 km (Silva Dias et al., 2005).

In the Amazon region of the Andean countries (Peru, Bolivia, Ecuador and Colombia), according to Villar et al. (2009), precipitation tends to decrease with surface height, but the wind direction patterns in this region hinder the determination of a simple relation between precipitation and altitude. Using 391 surface meteorological stations, the authors observed that few stations located at sea level heights above 2000 m presented annual values of precipitation higher than 1500 mm, while for stations located above 3000 m, annual precipitation was below 1000 mm. Among the analyzed stations, a high variability of precipitation accumulation was observed between neighboring stations, with differences that ranged from 250 to 6000 mm/year. In regions at lower altitudes, the highest precipitation accumulations were observed in the windward stations, while at higher altitudes, leeward stations showed higher accumulations.

The diversity of the precipitation systems makes knowledge of the cloud vertical structure particularly important for numerical modeling, precipitation forecasting and prediction of weather systems (Fall et al., 2013). Microphysical and macrophysical cloud parameters such as the liquid water path (LWP) and ice water path (IWP) are likely to present different values according to the region of study and therefore can help in the understanding and improvement of rainfall estimation. According to Iguchi et al. (2015), the uncertainty in the conversion from radar reflectivity to precipitation rate is one of the main sources of errors in the estimation of precipitation using the Tropical Rainfall Measurement Mission (TRMM) Precipitation Radar (PR). This uncertainty is related to variations in the droplet size distribution (DSD), which changes according to the region, season and rain type.

The ice water content and particle habits may be used as an indicator of its precipitation potential. Because of the higher and variable surface emissivity, high-frequency channels are more frequently used to estimate rainfall over land (Gopalan et al., 2010). The precipitation estimation using these channels is based primarily on brightness temperature depression caused by ice scattering, coupled with a relationship between the ice aloft and the surface rain rate. For passive microwave rainfall estimation over land, the rainfall rate to IWP thus becomes the single largest source of uncertainty.

There are different types of clouds where the ice content in the cloud top is not directly associated with the precipitation rate at the surface level, either due to low ice concentration and a high precipitation rate or due to high ice content and a low precipitation rate. This work aims to assess the robustness of ice-precipitation relations over different regions and seasons as well as the uncertainty in the estimation of precipitation and ice content estimators.

2. Data and methodology

The present study uses Global Precipitation Measurement (GPM) mission satellite data made available by the Colorado State University (CSU). Version 5 (V05) of the Dual-Frequency Precipitation Radar (DPR) and the GPM Microwave Imager (GMI) are considered. The period of study covers the period from September 2014 to August 2015.

The geographic area of study (Figure 1) was subdivided into smaller areas based on the acting precipitation systems, the topographic characteristics (The United States Geological Survey – USGS dataset) and the precipitation regime. In areas 1 and 2, points over the ocean were also considered. Area 1 comprises the east coast of the northeastern region of Brazil, delimited by longitudes of 34° to 36° W. Area 2 is located in the interior of the Brazilian northeast, between the longitudes of 36° to 46° W. Area 3 comprises a large part of the Amazon region, ranging in length from 46° to 74° W. Finally, area 4 is comprised of part of the Amazon region and the Andean region, delimited by longitudes of 74° to 82° W. All areas are delimited by latitudes from 1° N to 9° S.

The GPM mission is a satellite constellation created with the objective of providing global coverage of precipitation observations every two to four hours. The core satellite, launched in 2014, carries active and passive microwave sensors on board. The passive sensor is the GPM Microwave Imager (GMI), with thirteen microwave channels, ranging in frequency from 10 to 183 GHz. The active sensor is the Dual-Frequency Precipitation Radar (DPR), consisting of a Ku (13.6 GHz) and Ka (35.5 GHz) band radars that provide precipitation measurements with higher resolution, accuracy and sensitivity than the TRMM PR (Iguchi, 2000). The Ku band in the DPR works in a similar way as the TRMM PR, while the Ka band identifies light rain and snowfall (Iguchi, 2000). In this manner, the combination of the Ku and Ka bands provides a more accurate estimate of the parameters associated with the droplet size distribution (DSD). According to Lee and Chandrasekar (2013), with the information in two separate frequencies, it is possible to determine two of the three DSD parameters, resulting in more reliable precipitation estimates.

Together, the GMI and DPR provide a unique capability for measuring precipitation either in rain or snow forms in conditions that have been difficult to detect by earlier instruments. This is a consequence of the addition of high frequency channels (165.6 and 183.3 GHz) in the GMI instrument, as well as the inclusion of the Ka band radar in the DPR (NASA, 2017). The algorithms used in this work are described in subsections below.

The GMI and CMB datasets used in this work were co-located and had parallax errors corrected. The variables used to assess the variability of the radiative characteristics according to each region were the ice water path and the rainfall rate (RR) from the CMB dataset, and the reflectivity vertical profile from DPR and the brightness temperatures from the GMI dataset.

2.1 Combined radar-radiometer (CMB) algorithm

The combined use of active and passive microwave sensor data provides complementary information on the macrophysics and microphysics of precipitating clouds that can be used to reduce the uncertainties in combined algorithms for the retrieval of radar/radiometer data. In other words, combined algorithms use the radiometer signal as an alternative to the attenuation observed by the radar.

Combined retrievals produce a profile of hydrometeors, droplet size distribution and surface parameters for which the brightness temperature and reflectivity are consistent with the satellite measurements. These combined products can be used as Bayesian datasets for subsequent retrievals from multiple radiometers.

The operational combined algorithm was designed to reduce the uncertainties in the rainfall estimation by GPM, effectively integrating the supplementary information from the DPR and GMI in a consistent precipitation product. Although similar in many ways to previously developed combined algorithms, the GPM combined algorithm (CMB) had many resources specifically designed to meet GPM objectives, based on accurate and physically consistent precipitation estimates from several instruments and reanalysis of environmental data. The algorithm includes a structure for estimation based on a statistical formulation of the Gauss-Newton method, a parameterization for the nonuniform distribution of the precipitation within the radar field of view, a methodology to detect and explain the multiple dispersion in the observations of the Ka band radar (KaPR), and a statistical deconvolution technique that allows for an efficient sequential incorporation of radiometer information into DPR precipitation retrievals (Greco et al. 2016).

2.2 Passive microwave algorithm

Although chosen due to their sensitivity to the presence of hydrometeors in the atmospheric column, only a limited number of microwave radiometer channels are employed for quantifying rainfall rates from passive microwave retrievals over land. The reason lies in the high variability of the surface emissivity, which effectively masks the precipitation processes at lower frequencies (e.g., below 37 GHz), making differentiating between signal and noise extremely

hard for the algorithm. Thus, any attempt to use a full set of the sensor's channels with the goal of extracting more accurate information on hydrometeor profiles is typically unsuccessful. A solution to this problem is found in limiting the choice of radiometer channels to those not affected by surface properties. Thus, in the case of the TMI, only the 85 GHz V/H channels are used by the TRMM Mission (add reference). The brightness vector used for the profile retrieval thus has only 2 dimensions. For the GMI, it is possible to use more than 2 channels because the GMI carries four additional high frequency millimeter-wave channels ranging from 166 to 183 GHz.

The quality of the retrieved profiles strongly depends on the quality of the a-priori cloud structures that feed the radiative transfer code. To improve the quality of these database, some studies created a hybrid database using PR reflectivity profiles and numerical simulations (Kummerow et al., 2011; Viltard; Burlaud and Kummerow, 2006). PR profiles add realistic characteristics to the database, but with a deficient ice representation. This deficiency is partly due to the poor performance of the cloud models in the simulation of the different types of ice (hail, snow, etc.).

In the case of algorithms that use passive microwaves to estimate precipitation, the best known and used is the Goddard profiling algorithm (GPROF - Kummerow et al., 2001). GPROF V03 (version 03) was implemented at the launch of the GPM mission, based on datasets from TRMM, CloudSat, surface radars and models. Version V04 used GPM-generated data, but studies showed that the algorithm significantly overestimated the precipitation over the continents. In GPM V05 GPROF, which uses CMB V04 and DPR-Ku, there was an improvement in the ice hydrometeor simulations to obtain better agreement between the calculated and simulated bright temperatures. This resulted in lower brightness temperature adjustments between the radiometer simulations and a better consistency between the estimates from the radiometers and the combined products, as well as with validation surface data (NASA, 2017). Current GPROF versions of GPM use hydrometeor profiles from the DPR combined algorithm (Greco et al., 2016). Simulated brightness temperatures are obtained from a radiative transfer model, guaranteeing good agreement with GMI-observed Tbs. For the construction of the GPROF a priori databases, this information is then combined with the Ku-DPR precipitation

rate and with complementary data, such as the surface type and atmospheric temperature at 2 m above the surface.

In this research, the IWP is estimated from an algorithm similar to that described by Zhao and Weng (2002) and Mattos and Machado (2011) but using GMI channels. For the calculation of the IWP, some parameters need to be determined, including the effective particle diameter (D_e). The parametrizations for the estimates of D_e and IWP values are determined by combining empirical and statistical methods expressed by:

$$D_e = a_0 + a_1 r + a_2 r^2 + a_3 r^3 \quad (1)$$

$$IWP = \mu D_e \rho_i (\Omega / \Omega_N) \quad (2)$$

where r is the scattering ratio between the 89 GHz and 166 GHz channels and a_0 , a_1 , a_2 and a_3 are the regression coefficients ($a_0 = -0.3003$; $a_1 = 4.3088$; $a_2 = -3.9826$; $a_3 = 2.7832$), which depend on the ice particle volumetric density (ρ_i , in kg m^{-3}). The parameters associated with the IWP calculation are μ , ρ_i , $\Omega_{89\text{or}166}$ and Ω_N , which are the cosine of the zenith angle, ice particle volumetric density, scattering coefficient in both channels and the normalized scattering coefficient, respectively.

For the calculation of the ratio between the channels of 89 and 166 GHz, which expresses the scattering caused by large particles, we use Eq. 3 shown below:

$$r(D_e) = \frac{\Omega_{89}}{\Omega_{166}} = \frac{\Omega_{N89}}{\Omega_{N166}} \quad (3)$$

where Ω_{89} and Ω_{166} are the scattering coefficients for the 89 GHz and 166 GHz channels, respectively. Similar to that presented by Weng and Grody (2000), the scattering coefficient for channels (Ω_{89} and Ω_{166}) is determined using the difference between the cloud base ($T_B(Z_b, \mu)$) and top ($T_B(Z_t, \mu)$) temperatures, normalized by the value of the cloud top temperature, expressed as:

$$\Omega(\mu) = \frac{T_B(Z_b, \mu) - T_B(Z_t, \mu)}{T_B(Z_t, \mu)} \quad (4)$$

where $T_B(Z_i, \mu)$ is a direct measure obtained by GMI sensors. The cloud top brightness temperatures for both channels (89 and 166 GHz) are obtained from the GMI, while the cloud base temperatures for the continent are estimated from the low frequency channels (23 and 36 GHz), also of the GMI, using the equations expressed by:

$$BT_{89} = 17.88 + 1.61BT_{23} - 0.67BT_{36} \quad (5)$$

$$BT_{166} = 37.78 + 1.69BT_{23} - 0.80BT_{36} \quad (7)$$

The empirical relation between D_e and r is used to determine the ice particle size, only considering values of the scattering coefficient (r) less than 0.8. Thus, the condition for a detectable cloud considers only temperatures at 183.3 GHz of less than 265 K. For a value of D_e less than (or greater than) 1 mm, the Ω_{166} (Ω_{89}) is used in Eq. (2); D_e , and ρ_i (920 kg m^{-3}) are also used, while Ω_N is determined by:

$$\Omega_{N89or166} = \exp[b_0 + b_1 \ln(D_e) + b_2 (\ln(D_e))^2] \quad (8)$$

where b_0 , b_1 , and b_2 are the regression coefficients that depend on the D_e value.

For $D_e \geq 1.0$ mm:

$$b_0 = -1.1930; b_1 = 2.0883; \text{ and } b_2 = -0.8575;$$

For $D_e < 1.0$ mm:

$$b_0 = -0.2945; b_1 = 1.3884; \text{ and } b_2 = -0.7536;$$

3. Results

The error in the precipitation estimate using passive microwave sensors has been studied by several authors (Petković and Kummerow, 2017; Petković et al., 2018; Costa et al., 2018), either in a given region of study or by comparing results for different regions. However, comparisons that evaluate the variability of the error according to the regional characteristics and the seasonal influences typically require a more detailed analysis. In this work, the results obtained from the analysis of the precipitation estimates by the GMI and CMB are discussed, as well as the probable causes for errors in the estimation of precipitation using passive microwave sensors.

3.1 Statistics of the observed precipitation type in each area of study and the seasonal influence

The statistics of occurrence by the region of study and season of the year (i.e., the season) for clouds of the stratiform type, deep convective type, shallow convective type and others, is presented in Table 1. For the rain type classification, the information contained in the CMB data was obtained using the methodology proposed by Awaka et al. (2016). According to the authors, the classification is made using two modules, which consists of the Ku-only and Ka-only modules and the combination of the two modules (dual-frequency module). The Ku-only and Ka-only classification modules use algorithms that are similar to the TRMM rain type classification algorithm 2A23 (Awaka et al., 2009). The dual-frequency classification module uses a new method called the measured dual-frequency ratio (DFR_m) method for rain type classification and the detection of bright bands.

In area 1, comprising the east coast of the northeastern region of Brazil, there is a predominance of shallow convective clouds during the JJA (June-July-August) and SON (September-October-November) seasons, likely associated with easterly waves. Winds perpendicular to the coast increase the water vapor flux convergence, thus favoring the formation of clouds on the northeast coast of Brazil. Conversely, during the DJF (December-January-February) and MAM (March-April-May) quarters, stratiform clouds prevail, related to the ITCZ that reaches its more

southerly position in March-April and to the UTCV. UTCV are climatologically located in the ocean during these two quarters but can influence the type of precipitation, depending on the location of the center. In this area, the rainy season takes place between January and June. These results corroborate the relative frequency of the precipitation rate calculated for each season in this area (Figure 2), which presents higher frequencies for low rainfall rates in the SON and JJA quarters (Figures 2a and 2d), associated with a higher occurrence of shallow convective systems. While the DJF and MAM quarters (Figures 2b and 2c) show a lower frequency of low precipitation rates, consequently a higher frequency of higher precipitation rates relate to a higher occurrence of deep convective systems and stratiform systems. In area 2, the interior of the Brazilian northeast, stratiform clouds dominate in the SON, DJF and MAM seasons, whereas during the JJA season, shallow convective clouds are more frequent. Palharini and Vila (2017) found similar results and associated this increase in shallow convective cloud frequency in the JJA quarter to the Hadley and Walker cell circulation pattern, which tends to inhibit the formation of deep convective systems. The increase in the occurrence of shallow convective systems reflects the increase in the relative frequency of low precipitation rates observed in Figure 3d. Despite the predominance of stratiform rain during the MAM quarter in this region, an increase in the deep convective cases is also observed, likely associated with the influence of the ITCZ and squall lines acting in the north of this area. This increase in the occurrence of deep convective systems causes an increase in the relative frequency of higher precipitation rates (Figure 3c). In area 3, central Amazon, stratiform rain dominates throughout the year, but there is an increase in deep convective cases during the JJA and SON seasons. These cases display a decrease in the frequency of low precipitation rates, usually associated with shallow convective systems, and an increase in the relative frequency of higher precipitation rates, being best observed in the SON season (Figure 4a). In this area, those seasons are considered the dry period, when there is a high concentration of biomass burning aerosols that typically form cloud and rain droplets through ice growing processes. These conditions favor deep convective clouds. In area 4, as was observed in area 3, there is a predominance of stratiform clouds in all seasons, without significant seasonal variations, in agreement with results shown by Villar et al. (2009). The variations in the relative frequency are more significant in SON and DJF, with the decrease in the occurrence of shallow convective systems resulting in an increase in the frequency of higher precipitation rates (Figures 5a and 5b). As presented in Table 1, there is a predominance

of stratiform rain. This type of rain has less vertical variability and comprises larger areas, leading to an almost constant precipitation rate and the avoidance of co-location issues, resulting in a smaller error in the precipitation estimates using passive microwave sensors.

3.2 Vertical structure analysis

The seasonal variations of the predominant precipitation type for each area of study and of the frequency of occurrence of each precipitation type have been discussed in the previous subsections. However, in addition to information on the type of precipitation, it is necessary to consider the vertical structure of clouds. To assess the vertical structure of clouds, the mean reflectivity profiles for each area, type of precipitation and season were generated using the CMB algorithm (Figure 6). The analysis of the cloud vertical structure by type of precipitation allowed for the examination of the variability of the cloud mean reflectivity vertical profile according to the area of study and season. In general, for shallow convective clouds, there was no variability in the mean vertical profile throughout the year, and for each area of study, differences in the reflectivity were observed only at the lowest levels, which are wider in areas 1 and 2 than in the other two areas. Regardless of the area of study, for deep convective clouds, more significant differences were observed in levels above 5 km in height, i.e., associated with the cloud ice content. In areas 1 and 4, the IWP values were larger during DJF, associated with the acting ITZC and UPCV in area 1 and to the ITZC and local warming in area 4. In area 2, the IWP values were larger during MAM, when the ITCZ is also of influence, particularly in the northern region of the area. In area 3, the largest IWP values were observed during SON, during the dry period, characterized by the formation of deep convective systems. In area 4, differences were observed for levels below 5 km as well, with reflectivity values larger during DJF and JJA. For the stratiform type precipitation, more significant seasonal differences were observed in areas 1 and 2. In area 1, during MAM, the mean profile for the stratiform precipitation type shows rather constant reflectivity up to 5 km height and higher reflectivity values above when compared to the profiles obtained for SON and JJA. In MAM, the stratiform clouds displayed a deeper layer with higher reflectivity values at levels close to 5 km in height than in other seasons, which are associated with a higher content of liquid water. According to Palharini and Vila (2017), stratiform rain can be mistaken with warm rain produced by shallow convective systems.

In area 2, for JJA, the mean vertical profile is associated with clouds with little ice and liquid water content and lower values of the reflectivity for the entire profile when compared with the profiles for the other seasons due to the decrease in the number of stratiform cases. On the other hand, for MAM, higher reflectivity values above 5 km height were observed, with little variation below that level, when compared to the JJA quarter.

In general, from the mean vertical profiles, it was not possible to extract striking characteristics that could explain the errors in the precipitation estimation using passive microwave sensors. It is then likely that the errors in the rainfall estimates are associated either with the IWP-RR relation or the IWP estimate by the GMI.

3.3 Assessment of the IWP_{CMB} - RR_{CMB} relation

To assess how the ice content and the precipitation rate on the surface ($IWP - RR$) relation works for the complete area, a mean RR value was calculated for each IWP class considered in the analysis of the estimates using CMB (Figure 7a). Higher values of RR_{CMB} are clearly correlated with the increase in IWP_{CMB} for the area of study, indicating a robust relationship between these variables. IWP_{CMB} values above 1 kg m^{-2} are limited to fewer than 1% of the occurrences. Values higher than this threshold occur less frequently and need to be analyzed carefully. Considering all the cases within the complete area of study, it is observed that the higher densities (Figure 7b) occur for the lower IWP_{CMB} values, which is expected. From this graph, it is also possible to evaluate that there is only a weak relationship between RR_{CMB} and IWP_{CMB} .

Analyzing the IWP_{CMB} - RR_{CMB} relation by season, it could be observed that for area 1, there were no significant values of IWP during the SON and JJA quarters due to the predominance of shallow clouds. A more direct relation between IWP_{CMB} and RR_{CMB} was observed for the MAM quarter regardless of the area of study (Figure 8c), proving the efficacy of this relation in the assessment of the precipitation estimates, in particular for this season. However, the variation of RR_{CMB} with IWP_{CMB} values was small for JJA, and there was no clear relation between the two variables (Figure 8d), in agreement with the results shown in Figure 6b, in which there was an increase in reflectivity values above 5 km for the stratiform type clouds, but for levels below this threshold, little variation between values for MAM and JJA quarters was observed.

The mean RR_{CMB} for each IWP_{CMB} class generated according to each precipitation type is presented in Figure 9. Because the means were calculated based on IWP_{CMB} classes, only stratiform and deep convective types were considered. For convective clouds, a sharp increase of RR_{CMB} was observed for IWP_{CMB} values of up to 4 kg m^{-2} , becoming smoother for higher values. In the case of stratiform clouds, a sharp increase of RR_{CMB} with IWP_{CMB} was observed for area 2, while for the other areas, the increase was smooth. IWP_{CMB} values of up to 2.5 kg m^{-2} were observed with frequencies higher than 1% in the dataset of the convective cases, which was considered a high value of IWP_{CMB} (Braga; Vila, 2014). For the stratiform cases, this value was reduced to 1.5 kg m^{-2} . In general, the IWP_{CMB} - RR_{CMB} relation was robust for most areas, season and type of precipitation, despite the spatial and temporal variability that was expected. Naturally, this analysis did not include warm cloud cases because they did not have ice for the IWP_{CMB} calculation. It is worth noting that there were variations in the ice clouds that caused errors in the precipitation estimate, although this relationship is very well established. If these relations are relatively robust, even when they present errors, and these errors do not justify the errors observed and discussed in the previous figures, what could be the error factor? The other hypothesis to be analyzed is that the error is then due to the differences in the calculation of the IWP by models that use the brightness temperature to estimate the IWP. The next step is therefore to evaluate the T_b -RR relationship. For the analysis, the brightness temperatures of the channel of 89 GHz will be used.

3.4 Assessment of the T_{b89} - RR_{CMB} relation

Figure 10 shows the mean values of the CMB precipitation rate estimate (RR_{CMB}) as a function of the GMI 89 GHz channel brightness temperature class (T_{b89}) and the occurrence density according to the T_{b89} and RR_{CMB} values for the entire study area and for the period of one year. Just as in the analysis of the IWP-RR relationship, a strong link between T_{b89} and RR_{CMB} exists. In general, a lower T_{b89} yields a higher cloud top and precipitation rate. However, once T_{b89} is below 244 K, the frequency of occurrence is less than 1%, and especially for T_{b89} below 180 K, there is an increase in variability of the mean of RR_{CMB} . The highest frequency of occurrence is observed in the interval between 244 K and 288 K (Figure 10b), but no significant variation in the mean RR_{CMB} is detected. Separating the cases according to the type of precipitation, in

stratiform and convective cases (Figure 11), it is observed that there is a greater range of mean RR_{CMB} values with a data sample frequency greater than 1% for stratiform cases (Figures 11a and 11b); however, for values of Tb_{89} below 230 K, it is not possible to observe a clear relation between the variables. For convective cases (Figures 11c and 11d), although a smaller interval had a data sample frequency greater than 1%, it is observed that there is a clear relation for values of Tb_{89} up to 180 K.

In addition to the evaluations that take into account the complete area of study and the precipitation type, it is also necessary to analyze the behavior of the Tb_{89} - RR_{CMB} relation for different study areas and seasons. It is observed that, regardless of the choice of study region, if focused only on the Tb_{89} range where the frequency of cases is highest, it is not possible to determine a linear relationship between Tb_{89} and RR_{CMB} , especially for areas 3 and 4. For area 1 (Figure 12b), there is practically no case with Tb_{89} less than 200 K. When the analysis of the relationship is made according to the study area and the season (Figure 14), it is observed that for area 1 (Figure 14a), only in the MAM quarter, probably due to the activity of the ITCZ in this area, the mean RR_{CMB} for Tb_{89} is lower than 270 K, but for a small data sample size, since for this area the cases are concentrated between 270 and 290 K. Comparing the averages relationships between RR_{CMB} and Tb for the period of one year (Figure 12b) with the averages obtained from the individual quarters (Figure 14a), it is possible to identify the contribution of the MAM quarter in the annual average. For area 2, the DJF and MAM quarters present higher mean values of RR_{CMB} corresponding to colder Tb_{89} , whereas for the JJA quarter, where there is a greater frequency of shallow convective cases, Tb_{89} is limited to a minimum of 245 K (Figure 14b). In area 3 (Figure 14c), the highest averages are observed for the SON quarter, consistent with the period considered dry in the region where there is a higher concentration of aerosols and deep convective systems. In area 4, the observed differences are associated with the small increase in shallow convective clouds resulting in warmer Tb_{89} in the JJA quarter and colder Tb_{89} in the DJF quarter and the MAM quarter with higher RR_{CMB} averages. When analyzing the RR_{CMB} averages for the Tb_{89} classes according to the area of study, season and type of precipitation, it is possible to clearly verify that there are significant differences in the RR_{CMB} to Tb_{89} relationship, which leads to the conclusion that the algorithms used to estimate the precipitation rate do not take into account the seasonal variability related to the performance of a

given weather system. This leads to greater uncertainties in the precipitation estimates. The question that arises is: what would be the reason for this error? One hypothesis is that this error is associated with the relation between the ice water path (IWP) and precipitation rate (RR).

3.5 Assessment of the IWP

The mean IWP values obtained using GMI were generated for each IWP class obtained with CMB (Figure 15). Analyzing the plot of IWP_{GMI} versus IWP_{CMB} (Figure 15a) for the complete area, it is possible to see that IWP_{GMI} is relatively independent of IWP_{CMB} with an overestimation of IWP by Tbs for values lower than 1.2 kg m^{-2} , and an underestimation for higher values. The higher values observed in the complete area occurred with a lower frequency, below 1% for IWP values higher than 1.0 kg m^{-2} . Area 1 was not considered in the analysis because most of the area is composed of ocean. In Figure 16, where each area has an average value of IWP_{Tb} , it is observed that for area 2, the IWP_{CMB} values are overestimated for all classes of IWP_{CMB} , whereas for areas 3 and 4, this overestimation only occurs with values less than approximately 1 kg m^{-2} .

The differences between the IWP estimates made by CMB and Tbs appear similar to the errors found when comparing precipitation estimates by CMB and Tbs, showing that the IWP calculation by Tbs can be the primary cause of the difference between estimates by CMB and by Tbs. Our results show that errors in the precipitation estimate from passive microwave sensor data are mainly associated with the calculation of the ice content within the cloud and that the uncertainty in the estimate of the IWP directly influences the surface rainfall estimate. In the plots separated by season, it is possible to observe in detail how the error in the IWP estimate by GMI varies seasonally and regionally. The consequence is an overestimation for smaller values and an underestimation for higher values of the IWP (Figure 16). A similar result is found when the plots are separated by the precipitation type (Figure 17). For the stratiform cases, there is an overestimation regardless of the area of study (Figure 17b).

Although precipitation estimates obtained with the GMI algorithm proved to be accurate for some seasons of the year and some types of precipitation and an RR-IWP relation was verified, there were cases in which the GMI estimation presented larger errors, and this relation was rather

inefficient. This was probably due to the estimation of the ice content by T_{bs} , which typically overestimated the low values of the IWP and underestimated the higher values.

4. Conclusions

In this work, the regional and seasonal variability of the precipitation estimates obtained with the CMB algorithm were assessed. An initial analysis related to the precipitation regime of each study area showed that there was a significant variation of the predominant type of precipitation in each area associated with seasonal variability. However, the examination of the mean reflectivity profiles by area of study and precipitation type indicated that there were significant differences in the vertical structure that were associated with the precipitation type. The seasonal variability of the mean reflectivity profiles by type of precipitation was significant only for areas 1 and 2.

To understand the possible causes that could lead to errors in the estimates of surface precipitation obtained from passive microwave sensors, the relation between the precipitation rate and the ice content estimated by the CMB ($RR_{CMB}-IWP_{CMB}$) and the precipitation rate estimated by the CMB and the GMI ($RR_{CMB}-T_{b89}$) were analyzed. In general, the $IWP_{CMB}-RR_{CMB}$ relation was robust for most areas, season and type of precipitation, despite the spatial and temporal variability that was expected. While the $RR_{CMB}-T_{b89}$ relation was shown for higher T_{b89} values and using a larger data sample size, it was difficult to obtain a linear relationship between the variables; this relationship was observed only for colder temperatures but with a smaller data sample size.

The comparison between the IWP estimates (CMB and GMI) showed the most concrete differences, indicating that the errors in the precipitation estimation were related to the IWP estimation by the GMI. The results obtained after the analysis of the IWP estimate showed an overestimation of the IWP estimated by the GMI for the lower values, regardless of the area considered, and an underestimation for the higher values.

Acknowledgments: This research was supported by the SOS CHUVA FAPESP project 2015/14497-0. The authors acknowledge Colorado State University for providing the GPM data.

Table Captions

Table 1 - Precipitation classification statistics for each study area and quarter.

	Area 1			
	SON	DJF	MAM	JJA
Stratiform	34.7%	44.8%	48.8%	19.1%
Deep Convective	10.5%	20.6%	19.0%	13.2%
Shallow	54.8%	34.1%	32.0%	67.5%
Others	0%	0.5%	0.2%	0.2%
Total	352	563	1285	554
	Area 2			
Stratiform	66.7%	70.7%	53.6%	33.7%
Deep Convective	14.2%	17.0%	26.1%	21.4%
Shallow	18.5%	12.0%	19.7%	44.7%
Others	0.6%	0.3%	0.6%	0.2%
Total	666	5293	5685	1259

	Area 3			
Stratiform	66.9%	72.3%	72.2%	58.2%
Deep Convective	28.0%	19.8%	19.7%	33.1%
Shallow	4.7%	7.5%	7.7%	8.4%
Others	0.4%	0.4%	0.4%	0.3%
Total	13808	24491	32203	9387
	Area 4			
Stratiform	78.6%	72.9%	74.3%	70.7%
Deep Convective	16.6%	17.7%	15.9%	18.2%
Shallow	4.3%	9.1%	9.5%	10.9%
Others	0.5%	0.3%	0.3%	0.2%
Total	3471	5560	5645	3766

Figure Captions

Figure 1 – Selected study area in the tropical region of South America.

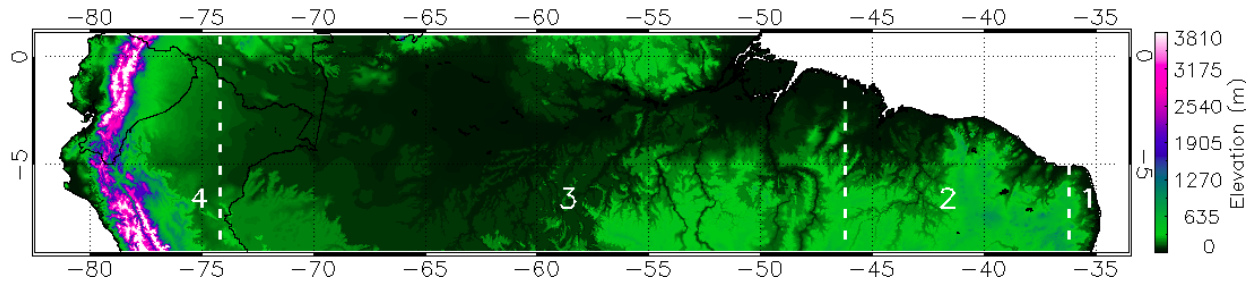


Figure 2 - Relative frequency of the rain rate for Area 1: a) SON; b) DJF; c) MAM and d) JJA.

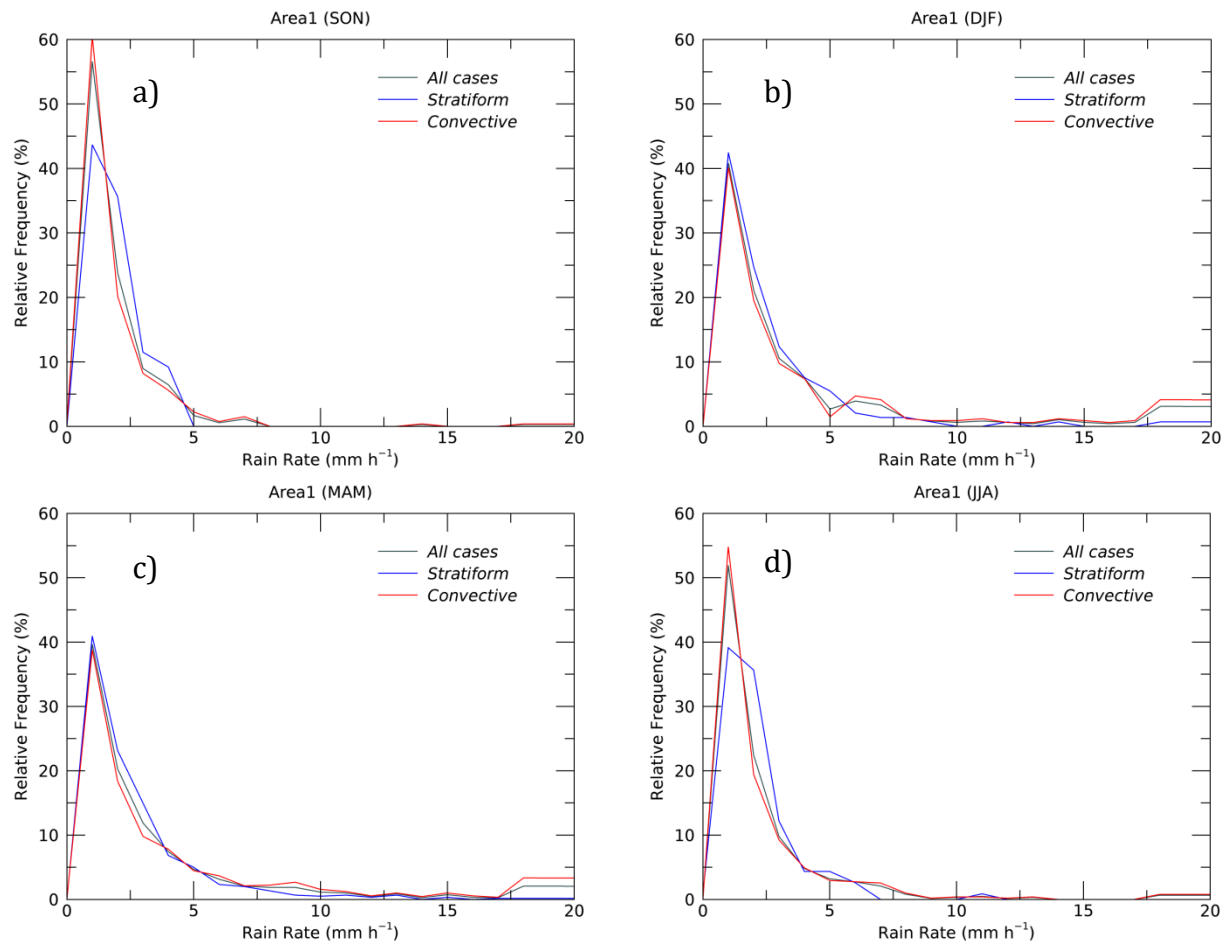


Figure 3 - Relative frequency of the rain rate for Area 2: a) SON; b) DJF; c) MAM and d) JJA.

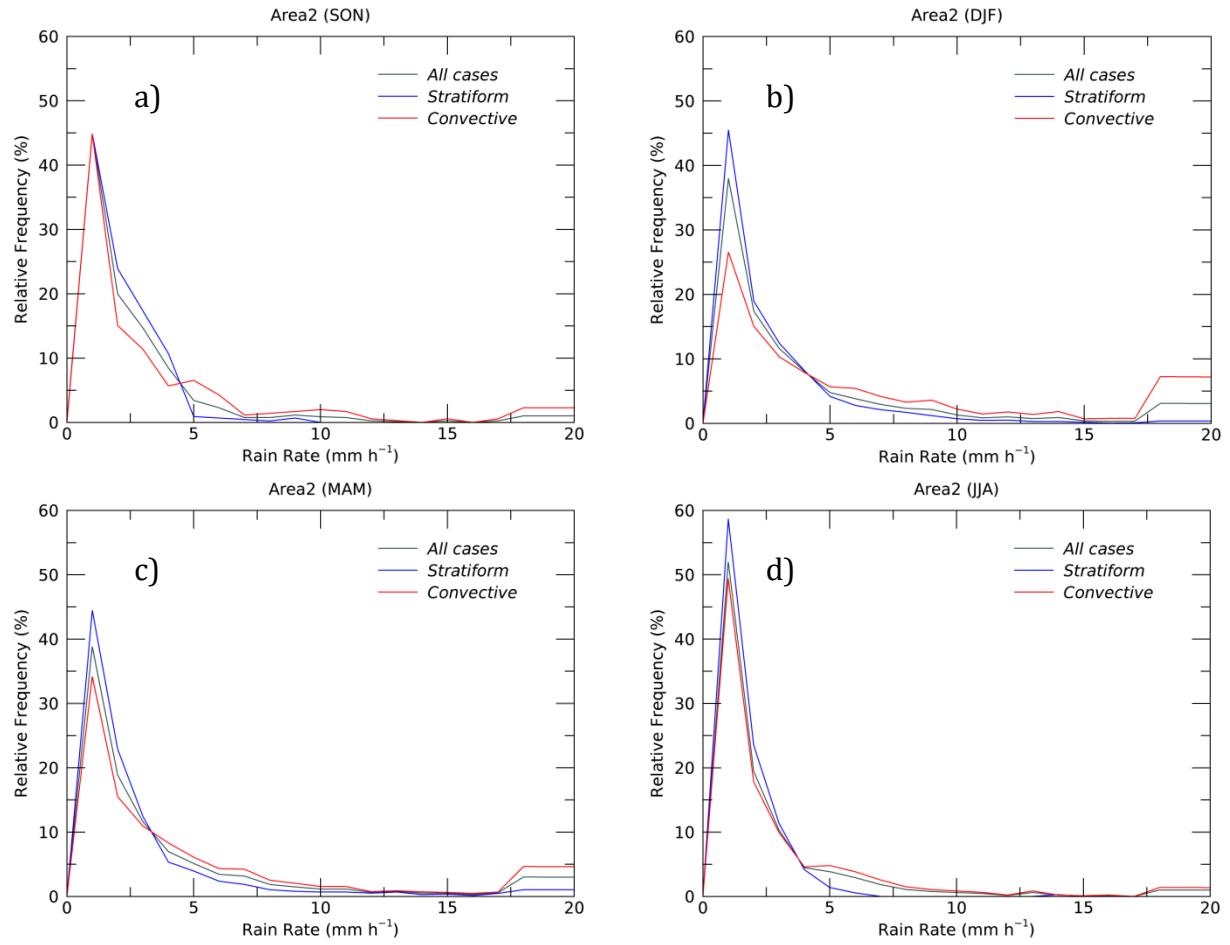


Figure 4 - Relative frequency of the rain rate for Area 3: a) SON; b) DJF; c) MAM and d) JJA.

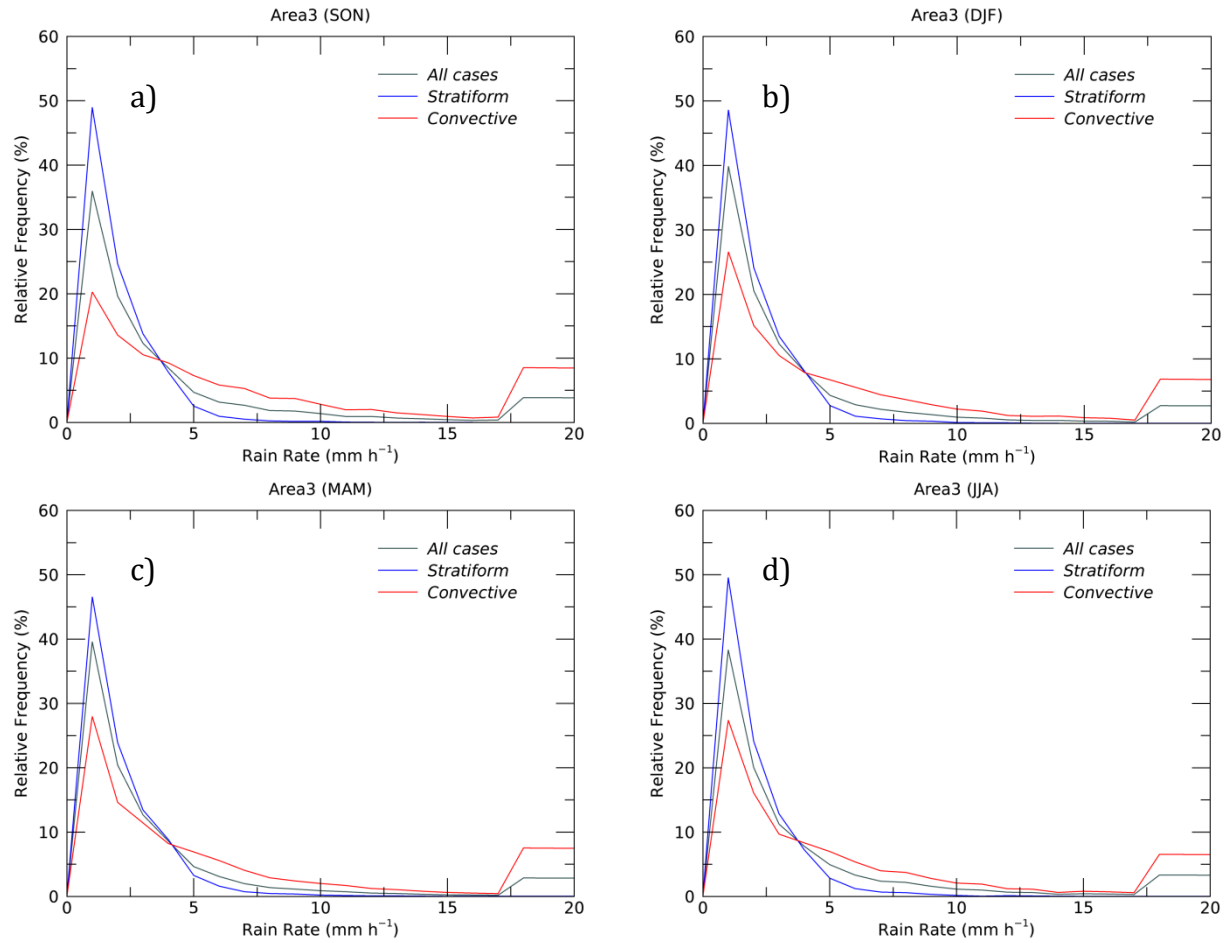


Figure 5 - Relative frequency of the rain rate for Area 4: a) SON; b) DJF; c) MAM and d) JJA.

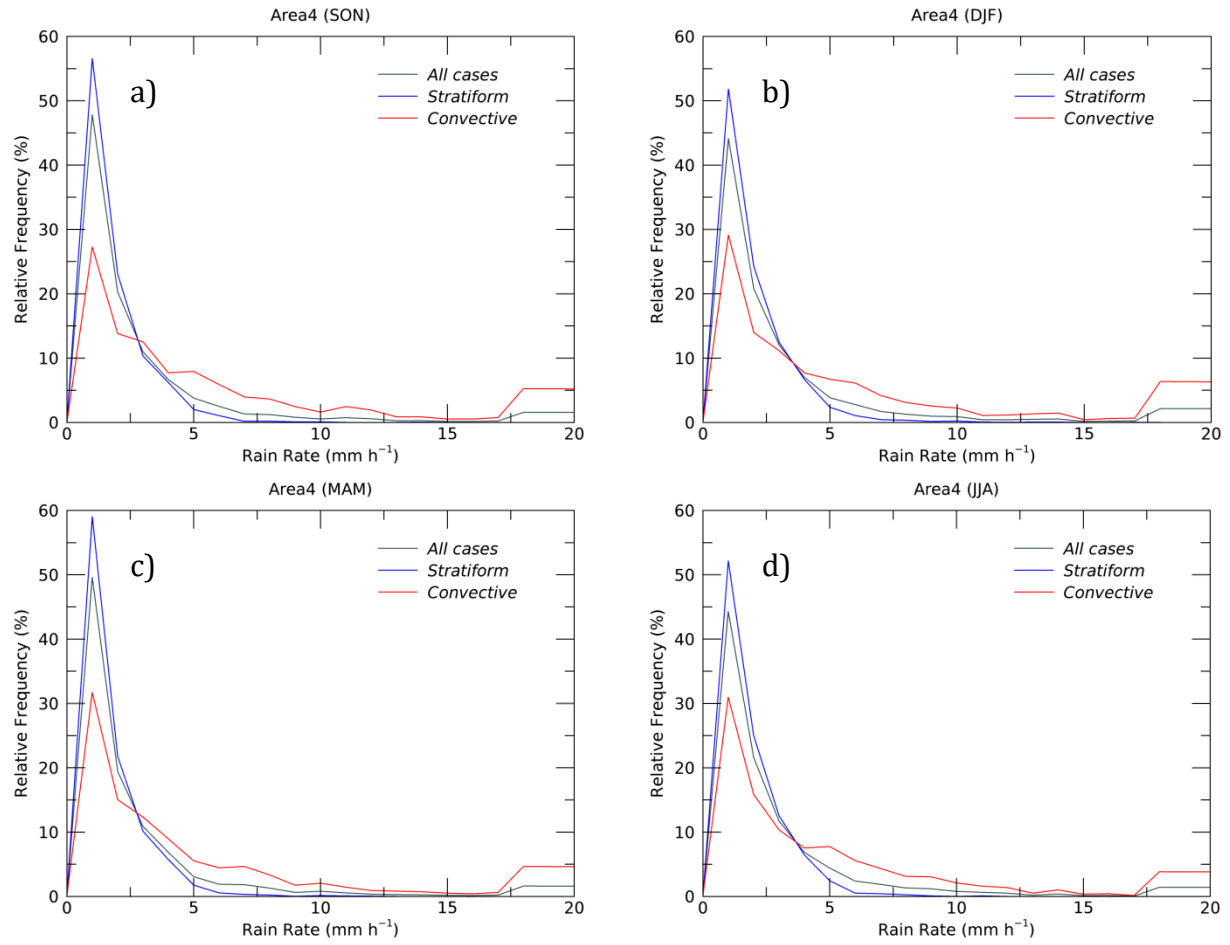


Figure 6 - Average profile of the reflectivity according to the rain type and the quarter of the year.

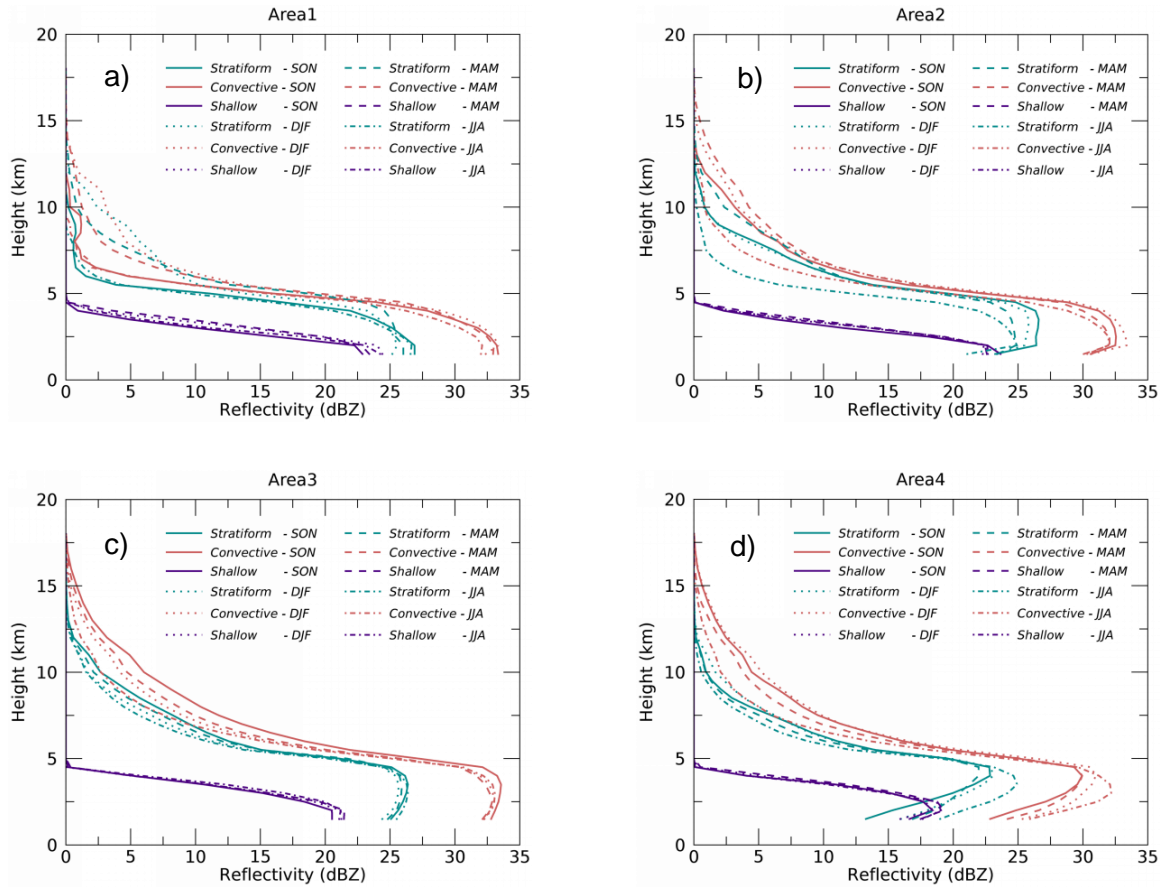


Figure 7 - a) Mean precipitation rate values estimated by CMB according to the IWP_{CMB} classes for the period of one year and for the complete area. The gray vertical line indicates the approximate class up to where the data sample frequency in each class is greater than 1%; b) Density according to the IWP and RR values.

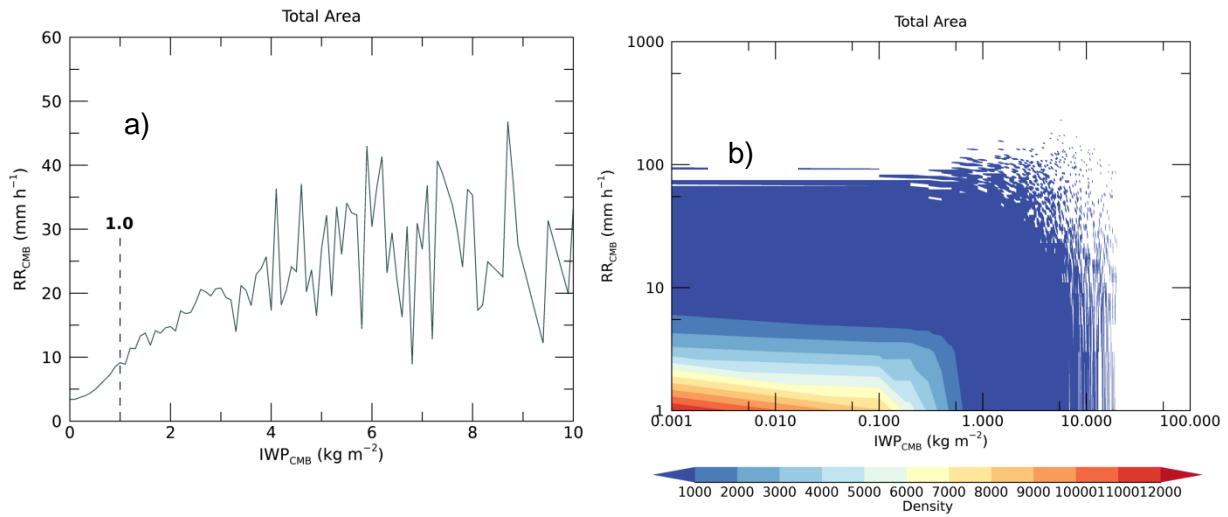


Figure 8 - Mean RR values estimated by CMB according to the IWP_{CMB} classes for: a) SON; b) DJF; c) MAM and d) JJA. The gray vertical line indicates the approximate class up to where the data sample frequency is greater than 1%.

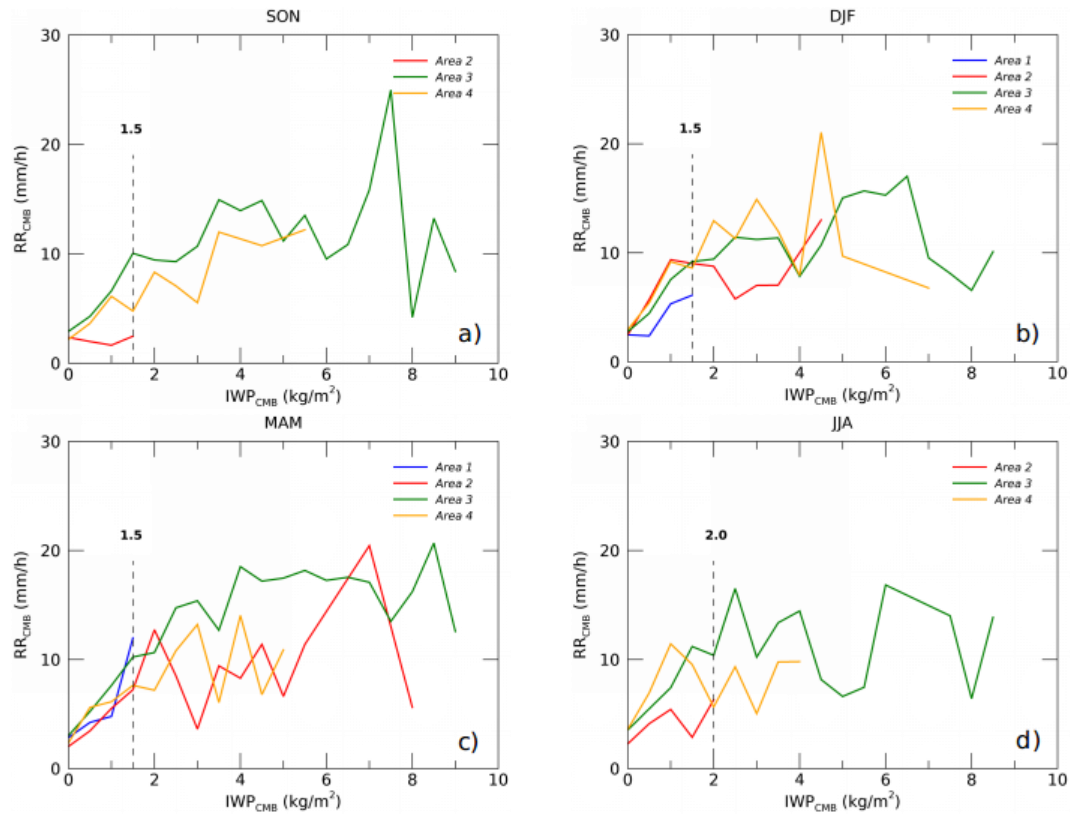


Figure 9 - Mean precipitation rate values estimated by CMB according to the IWP_{CMB} classes for all periods. a) Deep convective; and b) Stratiform cloud types. The gray vertical line indicates the approximate class up to where the data sample frequency is greater than 1%.

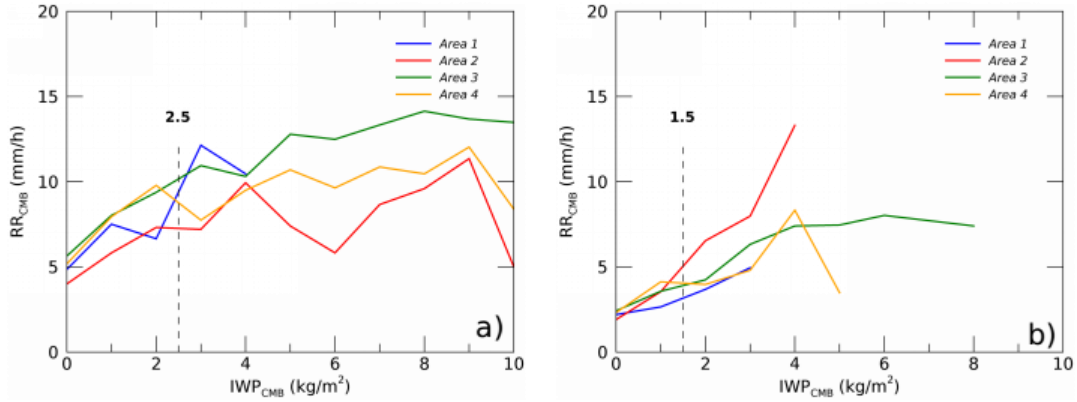


Figure 10 - a) Mean RR values estimated by CMB according to the Tb_{89} classes for the period of one year. The gray vertical lines indicate the approximate class interval where the data sample frequency is greater than 1%; b) Density according to the Tb and RR values.

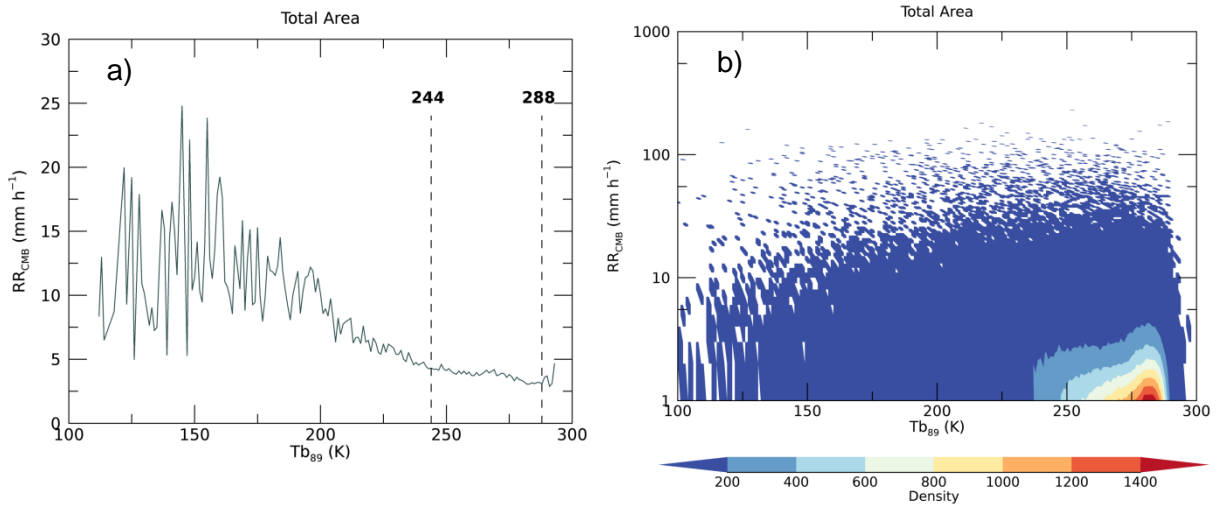


Figure 11 - a) and c) Mean RR values estimated by CMB according to the Tb_{89} classes for the period of one year and for stratiform and convective cloud types, respectively. The gray vertical lines indicate the approximate class interval where the data sample frequency is greater than 1%; b) and d) Density according to the Tb and RR values for stratiform and convective cloud types, respectively.

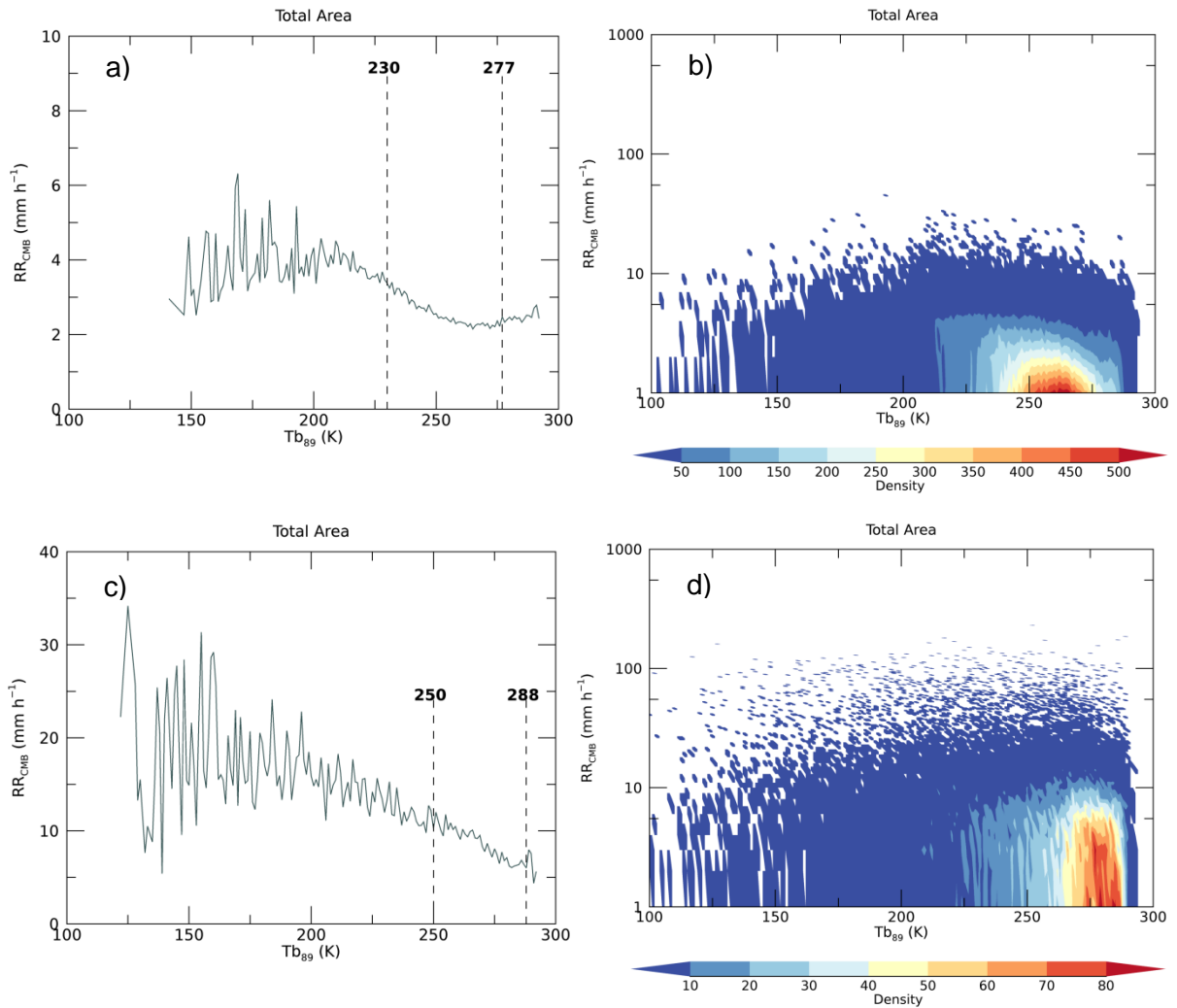


Figure 12 - a) and c) Mean RR values estimated by CMB according to the Tb_{89} classes for the period of one year and for Area 1 and Area 2, respectively. The gray vertical lines indicate the approximate class interval where the data sample frequency is greater than 1%; b) and d) Density according to the Tb and RR values for Area 1 and Area 2, respectively.

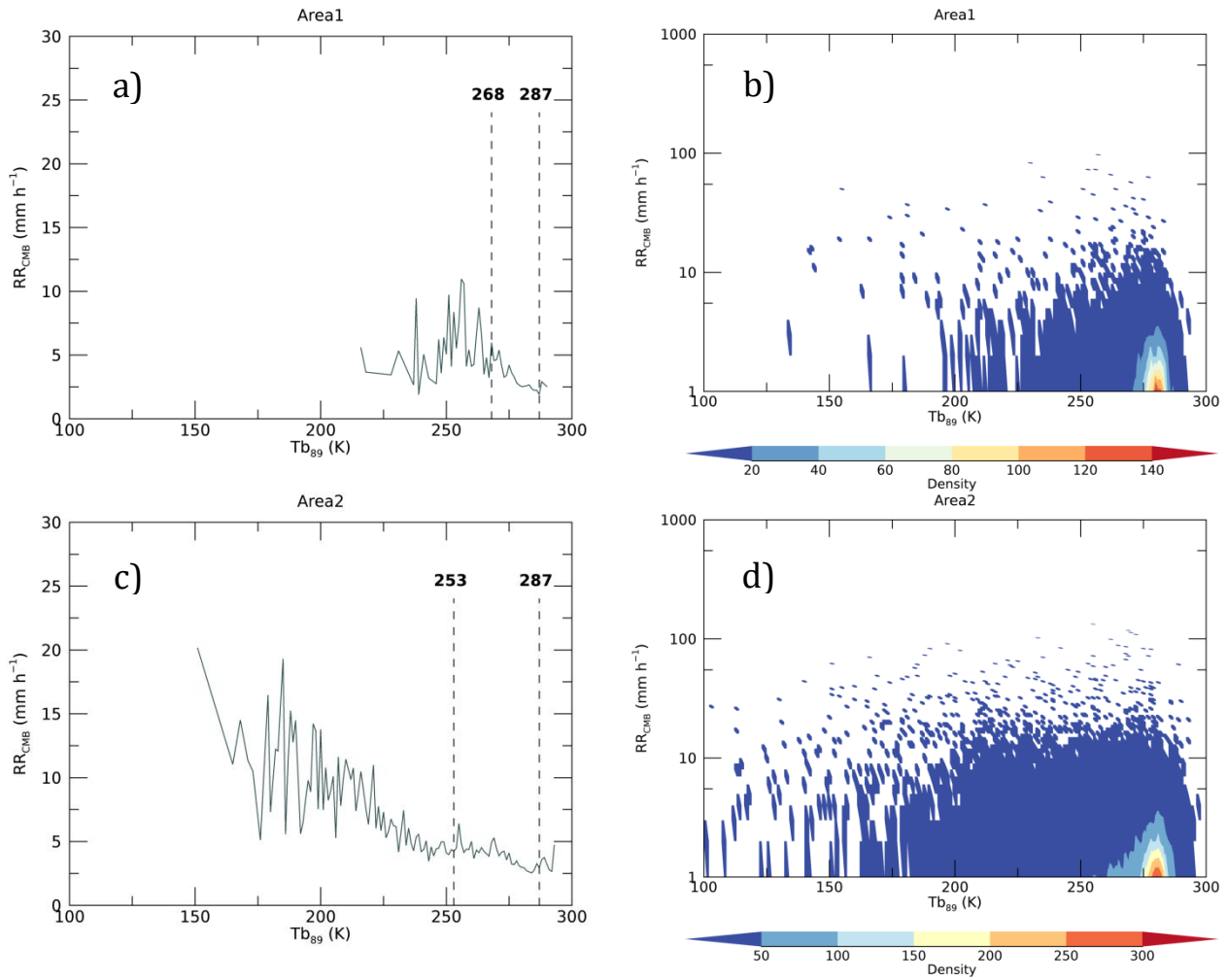


Figure 13 - a) and c) Mean RR values estimated by CMB according to the Tb_{89} classes for the period of one year and for Area 3 and Area 4, respectively. The gray vertical lines indicate the approximate class interval where the data sample frequency is greater than 1%; b) and d) Density according to the Tb and RR values for Area 3 and Area 4, respectively.

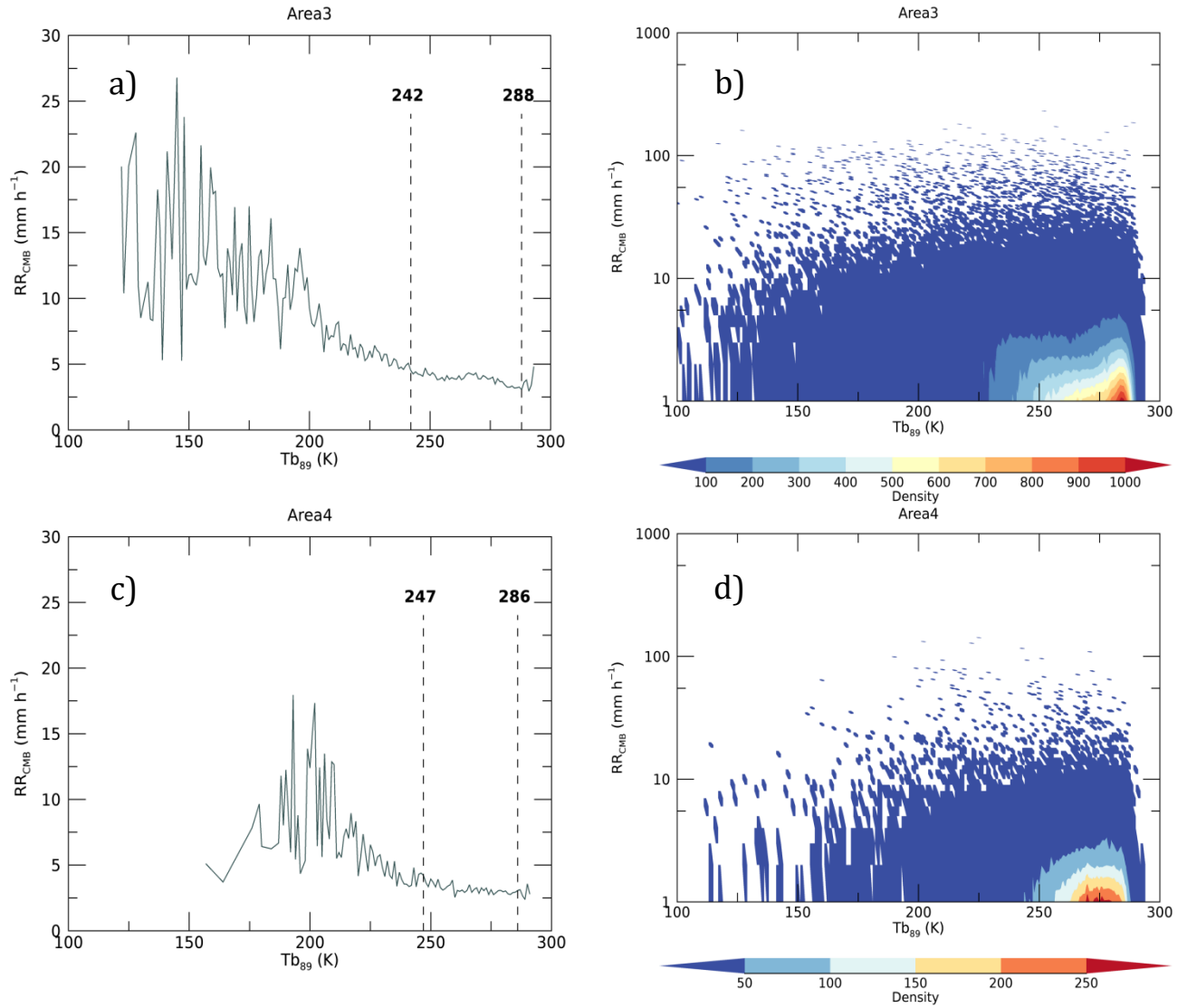


Figure 14 - Mean RR values estimated by CMB according to the Tb_{89} classes for the quarter of one year and for each area. a) Area 1; b) Area 2; c) Area 3; and d) Area 4.

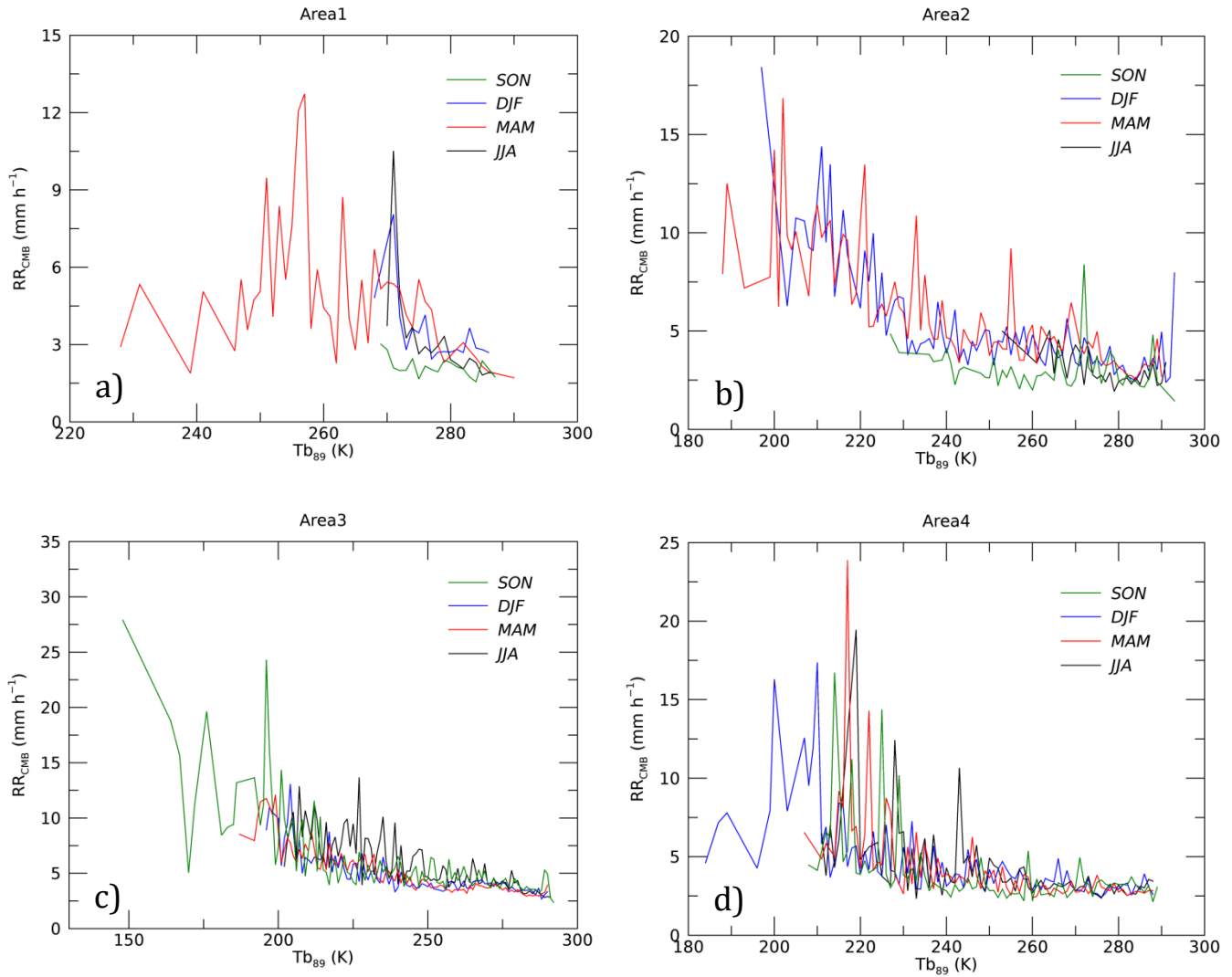


Figure 15 - a) Mean IWP values estimated by Tbs according to the IWP_{CMB} classes for the period of one year. The gray vertical line indicates the approximate class up to where the data sample frequency is greater than 1%. b) Density according to the IWP_{Tb} and IWP_{CMB} values.

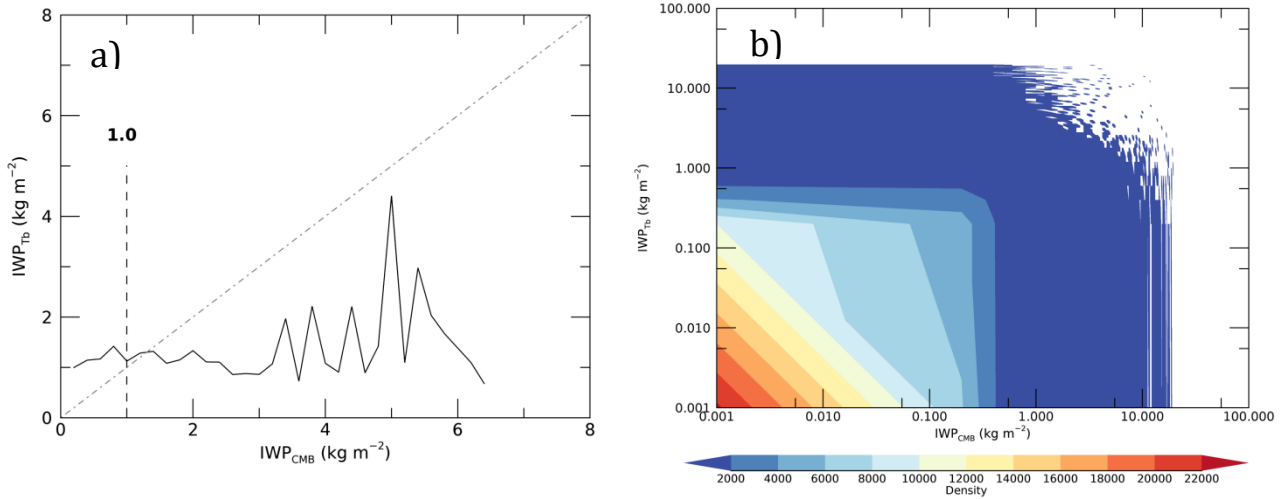


Figure 16 - Mean IWP values estimated by Tbs according to the IWP_{CMB} classes for the period of one year.

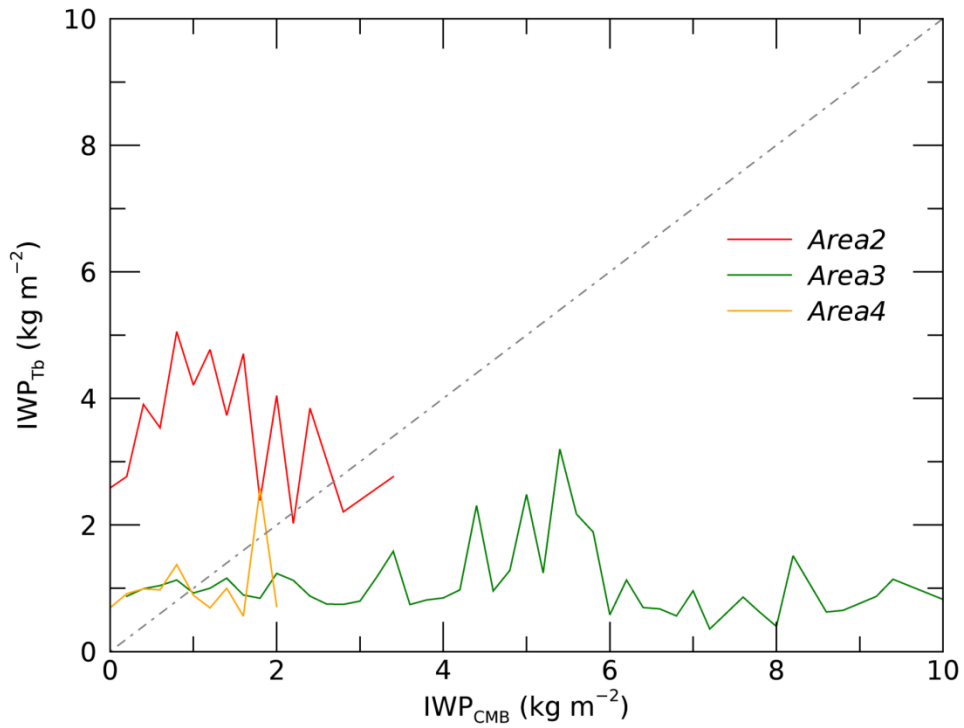


Figure 17 - Mean IWP values estimated by Tbs according to the IWP_{CMB} classes: a) Area 2; b) Area 3; and c) Area 4.

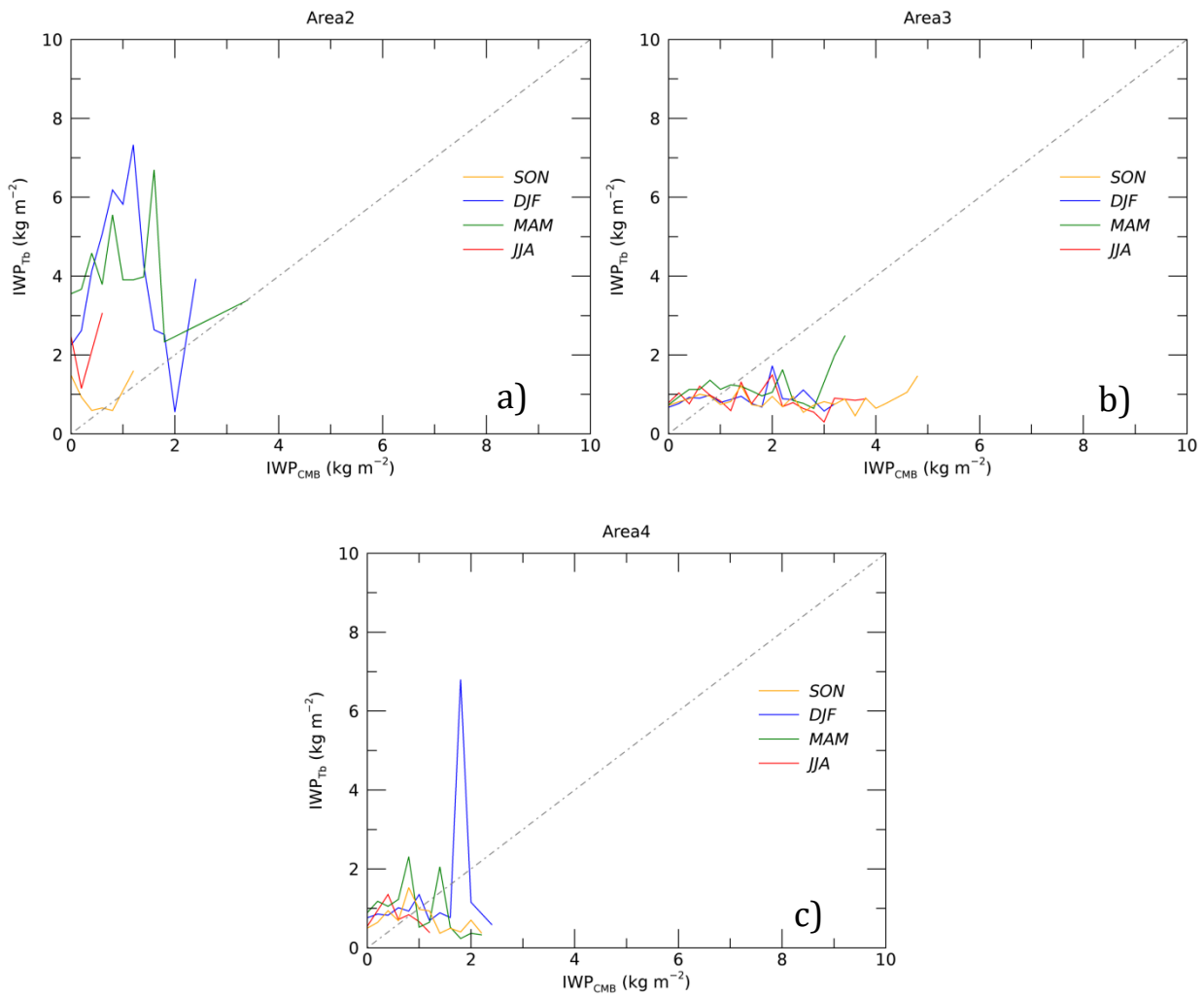


Figure 18 - Mean IWP values estimated by Tbs according to the IWP_{CMB} classes for all periods.

a) Convective; e b) Stratiform cloud types.

